Hemodynamic Alterations Associated with Coronary and Cerebral Arterial Remodeling Following a Surgically-Induced Aortic Coarctation

C. Alberto Figueroa, Jessica S. Coogan, Jay D. Humphrey

Abstract Computational models promise to aid in the interpretation of the coupled interactions between evolving wall geometry, structure, material properties and hemodynamics seen in arterial adaptations. Motivated by recent aortic coarctation models in animals, we used a computational fluid-solid-interaction model to study possible local and systemic effects on the hemodynamics within the thoracic aorta and coronary, carotid, and cerebral arteries due to a distal aortic coarctation and subsequent spatial variations in wall adaptation. In particular, we studied an initial stage of acute cardiac compensation (maintenance of cardiac output) followed by early arterial wall remodeling (spatially varying wall thickening and stiffening).

1 Introduction

Although elevated mean arterial pressure (MAP) has traditionally been considered to be an important indicator or initiator of cardiovascular risk in hypertension, mounting evidence suggests that increased pulse pressure is as or more important (Safar, 2000; Dart and Kingwell, 2001; Safar and Boudier, 2005). Data from surgically created aortic coarctations in animals reveal striking evolutions of wall geometry, structure, and properties (Xu et al., 2000; Hu et al., 2008; Eberth et al., 2010) that appear to be driven primarily by increased pulse pressure, not MAP (Eberth et

C. Alberto Figueroa
King's College London, London, SE16 7EH, UK
e-mail: alberto.figueroa@kcl.ac.uk

Jessica S. Coogan
Stanford University, Stanford, CA 94305, USA
e-mail: shihj@stanford.edu

Jay D. Humphrey
Department of Biomedical Engineering, Yale University, New Haven, CT 06520, USA
e-mail: jay.humphrey@yale.edu

al., 2009). It also appears that the associated arterial adaptations progress at different rates and to different extents both temporally (first at basal rates, then rapidly, then back to normal values) and spatially (from proximal to distal sites), see Hayenga (2010).

Although additional experimental data will be needed to understand better these spatio-temporal adaptations, computational fluid-solid-growth (FSG) models (Figueroa et al., 2009) offer considerable promise both in the design and interpretation of such experiments and in implicating possible biomechanical mechanisms.

Building on recent advances in computational modeling (Figueroa et al., 2006; Vignon-Clementel et al., 2006; Kim et al., 2009a,b; Moireau et al., 2012), the goal of this work was to simulate possible effects of a surgically created coarctation in the descending thoracic aorta on the hemodynamics within the proximal aorta and the coronary, carotid, and cerebral arteries following both an acute cardiac compensation (i.e., maintenance of cardiac output) and early arterial wall remodeling (i.e., spatially varying wall thickening and stiffening).

2 Methods

2.1 Model Geometry

2.1.1 Baseline Model

Computed tomographic (CT) images were collected from two adult male human subjects free of cardiovascular disease to collectively encompass all major arteries from the brain to the diaphragm. Separate 3D geometric models were constructed from the CT datasets using custom software based on a 2D vessel segmentation procedure, see Fig. 1. A finite element mesh was created by discretizing the 3D model coarsely, running a steady-state flow simulation, and then performing field-based adaptive mesh refinement (Sahni et al., 2006). The final finite element mesh consisted of $2,462,487$ linear tetrahedral elements and $477,872$ nodes.

2.1.2 Coarctation Model

A thoracic aortic coarctation was modeled by introducing a 75% diameter narrowing in the aorta just above the diaphragm, consistent with both the location and the degree of a surgically induced coarctation in mini-pigs in studies that provide information on temporal and spatial changes in arterial wall composition (Hu et al., 2008; Hayenga, 2010).
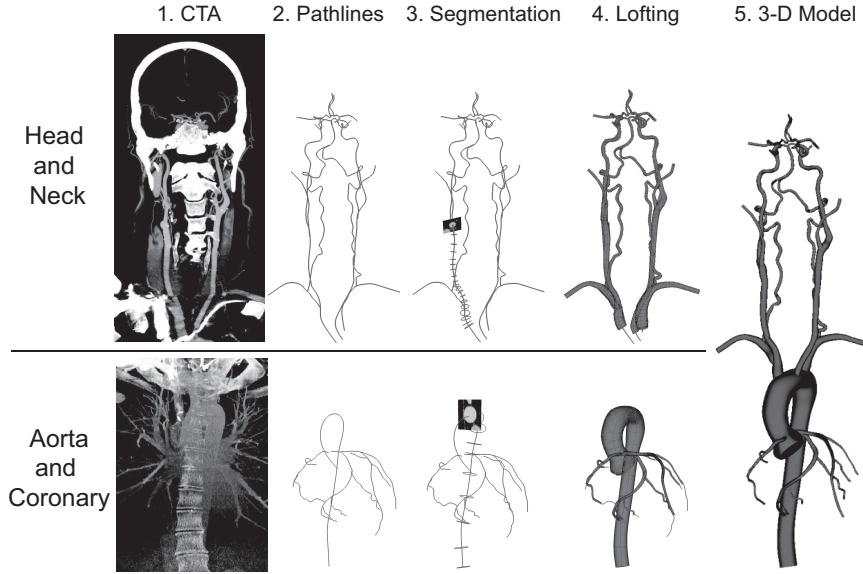
Fig. 1 3D computational model of the human thoracic aorta, coronary arteries, and head and neck vessels based on CT images from two normal male subjects. From Coogan et al. (2012).

2.2 Numerical Methods

Equations enforcing balance of mass and linear momentum (Navier-Stokes) were solved for the flow of an incompressible Newtonian fluid within a deformable domain using a stabilized finite element formulation implemented in the open-source code SimVascular (Figueroa et al., 2006). Computations were performed on a supercomputer (276 Dell PowerEdge 1950) typically using 96 cores. We utilized a time step size of 0.0001 seconds, and the simulations had an average residual of 0.005. Simulations were run for 7 cardiac cycles until achieving cycle-to-cycle periodicity in the pressure fields.

2.3 Fluid-Solid Models

Blood density was $\rho = 1.06 \, \mathrm{kg/m^3}$ and blood viscosity was $\mu = 0.04 \, \mathrm{P}$. We assumed typical baseline values for the linearized stiffness and thickness of the wall of each of the four primary vascular segments: thoracic aorta as well as coronary, neck, and cerebral arteries. A coupled momentum method was used (Figueroa et al., 2006) to model wall deformability and a coupled-multidomain formulation (Vignon- Clementel et al., 2006) was used to link Windkessel models for the heart and distal vessels to the 3D vascular model. The overall model thus required pre-

scription of one inlet and 22 outlet boundary conditions. Numerical values for the lumped-parameter coefficients were determined iteratively to reach target values for flow and pressure.

2.3.1 Heart Model

Overall function of the heart was simulated using a lumped parameter circuit model (Kim et al., 2009a) that includes resistors and inductors to represent the mitral and aortic valves (R_{AV}, R_{V-Art}, L_{AV}, L_{V-Art}), a pressure source that represents left atrial pressure P_{LA}, and a variable capacitance that represents left ventricular elastance/contractility $E(t)$, see Fig. 2. The initial left atrial pressure was assumed to be 10 mmHg. The final heart model parameters were $P_{LA} = 11$ mmHg, maximum elastance of 1.25 mmHg/mL, and time-to-peak elastance of 0.4 s. A Lagrange profile constraint with a penalty number of 10,000 was used to stabilize the solution during the systolic phase of the cardiac cycle (Kim et al., 2009b).

2.3.2 Windkessel RCR Model

Hemodynamic conditions were prescribed at every outlet in the descending aorta, neck, and head vessels in terms of a proximal (larger arteries and arterioles) resistance R_p, a proximal vessel capacitance C, and a distal (small arterioles and capillaries) resistance R_d (cf. Fig. 2). A Lagrange profile constraint was used at the inlet and outlet of the aorta as well as at the outlets of the right and left subclavian and external carotid arteries. Such constraints stabilize the computed solution while affecting only the hemodynamics in a small region near the constraint (Kim et al., 2009b).

2.3.3 Coronary Model

A lumped parameter model of the coronary vascular bed (Kim et al., 2010) was prescribed at the outlets of the large coronary vessels (cf. Fig. 2). In addition to the resistors and capacitance of the Windkessel model, this model included the venous circulation and incorporated effects of left ventricular pressure. The latter is critical since contraction of the heart is one of the main determinants of coronary flow. The total resistance at each outlet R_{total} was again calculated assuming a MAP of 100 mmHg and that flow through each outlet scaled with cross-sectional area, with mean coronary flow comprising approximately 4.5% of cardiac output (Guyton and Hall, 2006). The Windkessel portion of the lumped parameter coronary model was represented by R_a, C_a, and $R_{a-micro}$. The venous pressure defined the relationship between R_a, $R_{a-micro}$, and R_v and was assumed to be 15 mmHg. Two parameters, $C_{a-total}$ and $C_{im-total}$, were defined as the sum of all coronary arterial (C_a) and intramyocardial (C_{im}) compliances. An iterative tuning procedure was used to find values of $C_{a-total}$ and $C_{im-total}$ that yielded physiologic coronary flow waveforms. For the
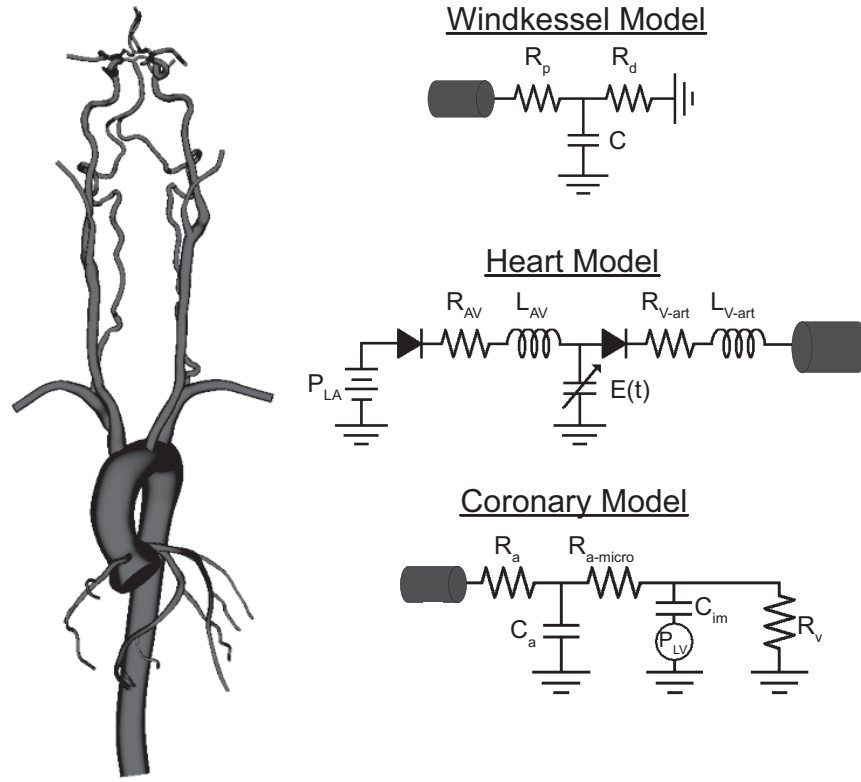
Fig. 2 Various lumped-parameter models utilized to specify boundary conditions for the 3D computational model. The Windkessel model was applied at all outlets except the coronary tree; the heart model was applied at the aortic root. From Coogan et al. (2012).

left coronary vessels, the left ventricular pressure found in the lumped parameter coronary model was equivalent to the pressure derived from the heart model. The boundary condition for the right coronary artery was based on a scaling of left ventricular pressure that was derived from the heart model, specifically $P_{RV} = 0.20 P_{LV}$. The final parameter values for the heart model and Windkessel models are listed in Table 1.

2.3.4 Vessel Wall Properties

Given current limitations in experimental data on regional variations in vascular mechanical properties and thickness, four sections of the vasculature were endowed with different but uniform wall properties, reflected by an effective constant stiffness and thickness of the wall (Fig. 3). The stiffness of the thoracic aorta was chosen to yield physiologic levels of strain over normal ranges of blood pressure (Redheuil et al., 2010) whereas moduli for coronary, neck, and cerebral vessels were

Windkessel Parameters				Coronary Parameters					
Outlet	R_p	R_d	C	Outlet	R_a	$R_{a-micro}$	R_v	C_a	C_{im}
Desc Aorta	0.25	2.48	500	LAD1	176	287	91	0.28	2.41
L Subclavian	1.88	19.0	44.7	LAD2	131	214	68	0.37	3.14
R Subclavian	1.88	19.0	48.3	LAD3	126	206	66	0.38	3.26
L Ext Carotid	4.39	44.4	15.0	LAD4	75	123	39	0.61	5.19
R Ext Carotid	4.39	44.4	13.9	LCX1	48	78	25	.07	9.17
L Ant Cerebral	11.2	113	5.23	LCX2	159	260	83	0.41	3.50
R Ant Cerebral	11.2	113	5.05	LCX3	213	348	111	0.32	2.78
L Int Carotid	3.18	32.1	11.0	LCX4	167	272	87	0.39	3.38
R Int Carotid	3.18	32.1	10.3	RCA1	166	271	86	0.59	5.07
L Post Cerebral	8.29	83.8	5.41	RCA2	231	377	120	0.44	3.74
R Post Cerebral	8.29	83.8	6.13	RCA3	258	422	134	0.39	3.38

Table 1 Parameter values for the lumped parameter Windkessel and coronary models. The unit of resistance is 10^3 dynes s/cm^5 and the unit of capacitance is 10^{-6} cm^5/dynes.

based directly on data (Gow and Hadfield, 1979; Hayashi et al., 1980; Nichols and O'Rourke, 2005). The thickness of the vessel in each section was assumed to be 10% of the mean radius within that section (Nichols and O'Rourke, 2005).

2.4 Acute Cardiac Compensation Following Coarctation

When first introducing the coarctation, parameters for the heart model were modified to simulate an acute cardiac compensation. This modification accounted for the increased work required of the heart to compensate for the increased afterload due to the coarctation. If the heart were not to adapt, then cardiac output would decrease due to the increased resistance in the aorta. Thus, the heart model was modified by iteratively increasing values of the maximum left ventricular elastance and left atrial pressure until cardiac output equaled that of the baseline model (Taylor and Donald, 1960). We assumed that cardiac output remained unchanged since the aortic stenosis was moderate and that it is unlikely that either the perfusion or the metabolic demands of the subject were altered significantly. It follows that, in order to maintain cardiac output, contractility of the heart (i.e., the elastance) must increase. In addition, changes in elastance affect filling of the heart, thus requiring an increase in left atrial pressure to maintain the same end diastolic volume. The final left atrial pressure was 14 mmHg and the maximum elastance was 1.52 mmHg/mL.

2.5 Early Arterial Remodeling

Early arterial vascular remodeling (i.e., within the first 10 days or so) was simulated by modifying wall properties to reflect stiffening and thickening of the thoracic aorta proximal to the coarctation, the coronary vessels, and the neck vessels.
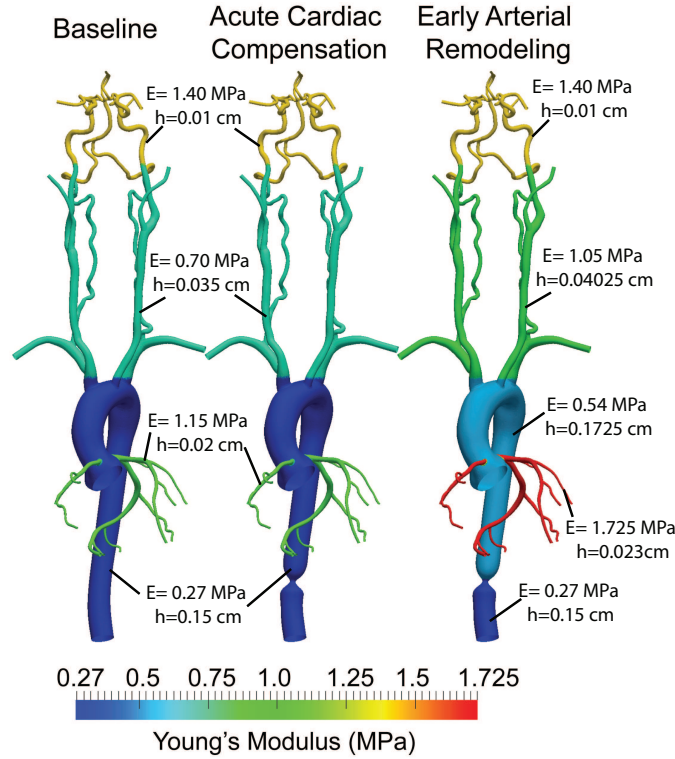
Fig. 3 Sections of the model with different wall properties. The acute cardiac compensation frame refers to the introduction of coarctation and subsequent cardiac compensation, the early arterial remodeling shows the differential stiffening observed in animal experiments in various vascular regions. From Coogan et al. (2012).

These changes were based on findings that the pulse wave velocity can increase by as much as two-fold with aging and that many adaptive processes associated with aging are similar to those associated with hypertension (Wolinsky, 1972; Nichols and O'Rourke, 2005). Updated values of stiffness and thickness are illustrated in Fig. 3. Briefly, the stiffness of the aortic arch, coronary tree, and neck vessels was increased by 100%, 50% and 50%, respectively, while the thickness was increased 15%. We assumed that the cerebral vasculature did not experience any changes in stiffness or thickness during this early period (Hayenga, 2010). We also did not prescribe any associated changes in vascular lumen largely because of the lack of associated experimental data and the possible competing effects of changes in distal resistances (e.g., cerebral autoregulation) and local shear-regulated vasodilatation. The prescribed changes in vascular stiffness and thickness affected cardiac afterload, hence additional cardiac compensation was required to maintain cardiac output after arterial remodeling. The final left atrial pressure was 16 mmHg and the maximum elastance was 1.82 mmHg/mL. All other outlet boundary conditions (arterial and

coronary) remained the same for baseline, acute cardiac compensation, and early arterial remodeling.

2.6 Data Analysis

Simulation data were analyzed using the open-source software Paraview (Kitware, Inc. Clifton Park, NY). Pressure, flow, and cyclic wall strain were analyzed at five different locations within the vasculature (see Fig. 4): the proximal descending aorta (P-Ao), left anterior descending (LAD) coronary artery, left common carotid artery (LCCA), left middle cerebral artery (LMCA), and basilar artery (BA). Mean circumferential wall strain was calculated based on changes in the cross sectional area of the vessel over a cardiac cycle using the following Green-Lagrange type expression $E_{\theta\theta} = (A_t/A_D - 1)/2$, where A_t is the cross sectional area at any given time t and A_D is a reference diastolic value (note: using area effectively represents radius squared as needed in the nonlinear measure of strain).

3 Results

The baseline simulation provided a prototypical human aortic pressure of $120/80$ mmHg, cardiac output of 5 L/min, and heart rate of 60 bpm. Associated pressure, flow, and strain waveforms also had realistic shapes (see blue plots in Fig. 4). The P-Ao had the highest mean and peak strain, followed by the LCCA, BA, LAD, and LMCA. Conversely, the highest mean wall shear stress and mean circumferential stress were in the LMCA, followed by the BA, LAD, LCCA, and P-Ao. The coronary arteries exhibited realistic shapes and averages in the flow, pressure, and strain waveforms. In addition, equal regional blood flows were obtained in the left and right cerebral hemispheres, with mean and pulse pressure lower in the cerebral arteries than in other areas of the vasculature. These results are summarized in Fig. 4 and Table 2.

Cardiac output would have decreased from 5 to 4.46 L/min after introducing the 75% aortic coarctation if no changes were made in the lumped parameter heart model. Increasing the maximum elastance of the heart from 1.25 to 1.52 mmHg/mL maintained cardiac output at 5 L/min, but increased blood pressure in the entire model (e.g., from $120/80$ to $\approx 150/90$ mmHg in the P-Ao). The pressure, flow, and strain waveforms exhibited more oscillations in each vascular territory, possibly due to the additional reflection site at the coarctation (Fig. 4). Similar to the baseline condition simulation, the P-Ao had the highest mean and peak strain, followed by the LCCA, BA, LAD, and LMCA, all with values higher than in baseline conditions. Interestingly, while the % increase in MAP was approximately the same throughout the model; the % increase in pulse pressure was greatest in the P-Ao, followed by the LCCA, BA, LAD, and LMCA (Table 3). Whereas flow increased through
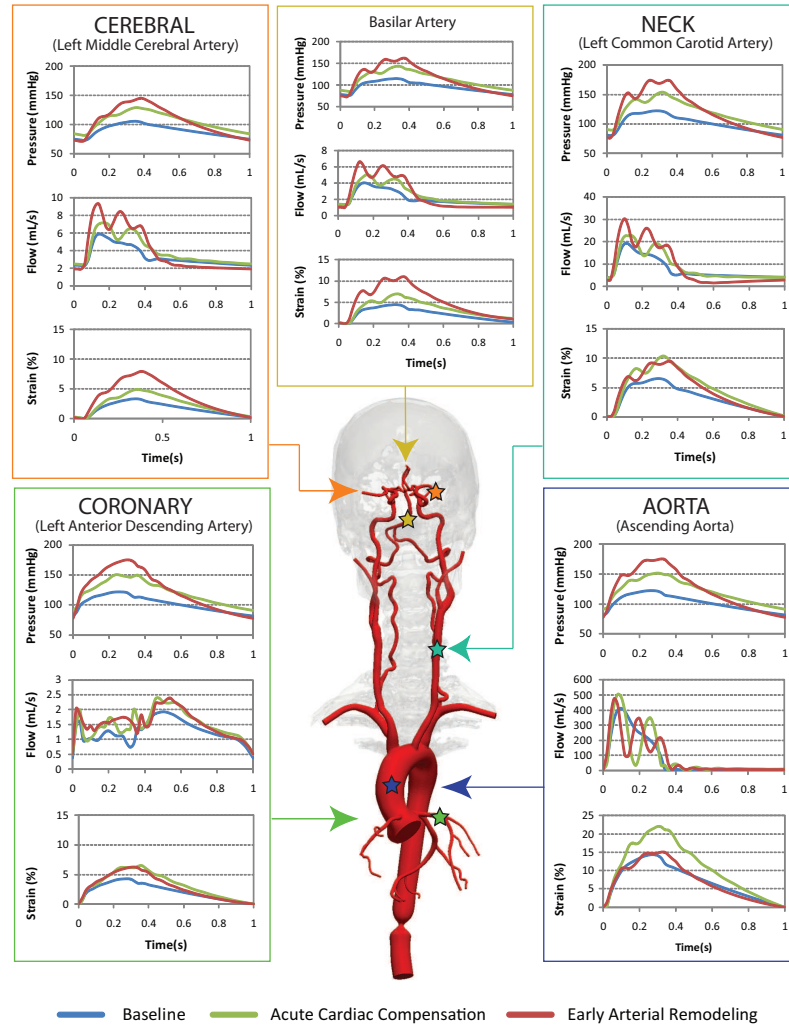
Fig. 4 Pressure, flow, and wall strain in baseline, acute cardiac compensation, and early arterial remodeling conditions. From Coogan et al. (2012).

the LAD, LCCA, LMCA, and BA, it decreased in the P-Ao, thus indicating an early redistribution of flow due to the increased resistance at the coarctation. This redistribution also explained the smaller percentage increase in wall shear stress in the P-Ao compared to the other vascular territories. Cardiac workload, as measured by the area within the pressure-volume loop of the left ventricle, increased 17% from 8476 to 9890 mmHg/mL.

In the early arterial remodeling case, had the heart model not been modified, the changes in arterial properties would have decreased cardiac output from 5 to 4.59 L/min. Additional cardiac compensation was thus introduced (e.g., increased

	Baseline					Acute Cardiac Compensation				
	Aorta	LAD	LCCA	LMCA	Basilar	Aorta	LAD	LCCA	LMCA	Basilar
P_{mean} (mmHg)	102	102	101	89	96	121	121	120	105	114
PP (mmHg)	42	40	42	33	38	70	60	65	47	58
Q_{mean} (mL/s)	54.5	1.2	7.5	3.4	2.1	47.7	1.5	8.9	4.0	2.5
$E_{\theta\theta}^{\text{mean}}$ (%)	5.9	2.2	3.2	1.7	2.3	8.9	3.2	4.8	2.4	3.6
$E_{\theta\theta}^{\text{peak}}$ (%)	12.0	4.3	6.6	3.4	4.5	20.6	6.6	10.3	4.9	7.1
τ_{mean} (Pa)	0.98	1.12	1.11	9.57	3.59	1.01	1.40	1.41	11.82	4.56
σ_{mean} (kPa)	94	153	141	164	204	112	182	167	193	242

	Early Arterial Remodeling				
	Aorta	LAD	LCCA	LMCA	Basilar
P_{mean} (mmHg)	124	124	123	106	116
PP (mmHg)	101	97	97	74	88
Q_{mean} (mL/s)	45.6	1.5	9.0	4.0	2.6
$E_{\theta\theta}^{\text{mean}}$ (%)	5.8	2.9	4.4	3.7	5.3
$E_{\theta\theta}^{\text{peak}}$ (%)	12.6	6.2	9.5	8.0	10.9
τ_{mean} (Pa)	0.78	1.43	1.58	12.58	4.91
σ_{mean} (kPa)	100	162	149	195	247

Table 2 Results for the three simulated stages: P_{mean} = mean arterial pressure; PP = pulse pressure; Q_{mean} = flow; $E_{\theta\theta}$ = cyclic strain; τ_{mean} = wall shear stress; σ_{mean} = circumferential wall stress.

	Baseline vs. Acute (%)					Baseline vs. Early Remodeling (%)				
	Aorta	LAD	LCCA	LMCA	Basilar	Aorta	LAD	LCCA	LMCA	Basilar
ΔP_{mean}	19	19	19	18	19	22	22	22	19	21
ΔPP	67	26	55	42	53	140	143	131	124	132
ΔQ_{mean}	−12	26	19	16	19	−16	28	20	19	24
$\Delta E_{\theta\theta}^{\text{mean}}$	51	45	50	41	52	−2	32	38	118	130
$\Delta E_{\theta\theta}^{\text{peak}}$	72	53	56	44	58	5	44	44	135	142
$\Delta\tau_{\text{mean}}$	3	25	27	24	27	−20	28	42	31	37
$\Delta\sigma_{\text{mean}}$	19	19	18	18	19	6	6	6	19	21

	Acute vs. Early Remodeling (%)				
	Aorta	LAD	LCCA	LMCA	Basilar
ΔP_{mean}	2	2	3	1	2
ΔPP	44	62	49	57	52
ΔQ_{mean}	−4	2	1	2	4
$\Delta E_{\theta\theta}^{\text{mean}}$	−35	−9	−8	54	51
$\Delta E_{\theta\theta}^{\text{peak}}$	−39	−6	−8	63	54
$\Delta\tau_{\text{mean}}$	−23	2	12	6	8
$\Delta\sigma_{\text{mean}}$	−11	−11	−11	1	2

Table 3 Percent changes between baseline and acute cardiac compensation, baseline and early arterial remodeling, and acute cardiac compensation and early arterial remodeling.

maximum elastance to 1.82 mmHg/mL) to maintain cardiac output at 5 L/min. This change resulted in yet another increase in blood pressure throughout the model, with aortic blood pressure reaching $\approx 180/80$ mmHg. Additional oscillations were seen in the pressure, flow, and strain waveforms compared with those found in the acute cardiac compensation stage (Fig. 4). The P-Ao again had the highest mean and peak

strain, followed by the BA, LCCA, LMCA, and LAD. In this case, wall strain returned to near baseline levels in the P-Ao, whereas strains in the LCCA and LAD were approximately the same as for acute cardiac compensation despite the stiffening and thickening experienced by these arteries. Lastly, strains in the LMCA and BA were higher than those seen with acute cardiac compensation due to the higher mean and pulse pressures, but no changes in wall properties. The mean values of circumferential stress were between those for baseline and acute cardiac compensation for the P-Ao, LCCA, and LAD, but higher in the basilar artery and LMCA. When comparing acute cardiac compensation and early arterial remodeling, the % increase in mean pressure was nearly identical throughout the entire model but the % increase in pulse pressure differed regionally, see Table 3. This finding emphasizes that possible differential changes in pulse, not mean, pressure throughout the vasculature might be responsible for different time courses of arterial remodeling. Flow through the LAD, LCCA, LMCA, and BA increased, whereas flow through the P-Ao decreased further. Cardiac workload increased 12% from 9890 to 11059 mmHg/mL.

4 Discussion

Findings over the past few decades have revealed that vessels within the elastic, muscular arteries, arterioles, capillaries, venules or veins respond markedly differently to altered biomechanical stimuli. For example, whereas all arteries and arterioles tend to thicken in response to hypertension, the elastic arteries, muscular arteries, and arterioles tend to do so while increasing, maintaining, and decreasing their caliber, respectively (Humphrey, 2002). More recently, it has become apparent that differential remodeling responses can even occur within vessels of the same general classification and within close proximity to one another. For example, the ascending aorta (an elastic artery) appears to be the first central artery (i.e., of the rest of the aorta and carotids) to manifest aging related changes in structure that affect overall mechanical properties (Redheuil et al., 2010). Amongst the many effects of aging on arteries, including increased endothelial dysfunction and advanced glycation endproducts (Lakatta et al., 2009; Safar, 2010), it appears that fatigue-type damage to elastic fibers is particularly important (Arribas et al., 2006; O'Rourke and Hashimoto, 2007). Indeed, it may well be that the increased susceptibility of the ascending aorta to an aging related loss of elastic fiber integrity may explain in part the increased susceptibility of the same region to dilatation and dissection in Marfan syndrome (Pearson et al., 2008), which results from a genetic mutation in the fibrillin-1 gene (FBN1); fibrillin-1 appears to help stabilize elastic fibers, hence mutations in FBN1 also result in decreased elastic fiber integrity.

Understanding better the spatio-temporal progression of vascular changes in both adaptive and maladaptive G&R could impact clinical care significantly. For example, being able to identify early indicators of vascular disease or subsequent risk could allow earlier interventions, before the subsequent disease presents symptomatically as heart attack, stroke, or other life threatening condition. A long-term

goal of this work is to build a new class of computational models that aid in understanding local and systemic effects of spatially and temporally progressive changes in large portions of the vascular tree and attendant changes in the hemodynamics, which in turn serve as strong mechanobiological stimuli for subsequent vascular growth and remodeling.

Toward that end, here we presented a zeroth order model wherein progressive changes in large segments of the vasculature were introduced based on limited observations in the literature to study possible consequences on the associated hemodynamics. Specifically, motivated by animal models of increased blood pressure/pulse pressure (Xu et al., 2000; Hu et al., 2008; Eberth et al., 2009; Hayenga, 2010), we studied the potential short-term effects of the abrupt creation of a 75% coarctation in the human descending thoracic aorta.

References

Arribas, S. M., Hinek, A., Gonzalez, M. C., 2006. Elastic fibres and vascular structure in hypertension. Pharmacol. Ther. 111, 771–791.

Coogan, J. S., Humphrey, J. D., Figueroa, C. A., 2012. Computational simulations of hemodynamic changes within thoracic, coronary, and cebrebral arteries following early wall remodeling in response to distal aortic coarctation. Biomech. Model. Mechanobiol., in press.

Dart, A. M., Kingwell, B. A., 2001. Pulse pressure-a review of mechanisms and clinical relevance. J. Am. Coll. Cardiol. 37, 975–984.

Eberth, J. F., Gresham, V. C., Reddy, A. K., Popovic, N., Wilson, E., Humphrey, J. D., 2009. Importance of pulsatility in hypertensive carotid artery growth and remodeling. J. Hypertension 27, 2010–2021.

Eberth, J. F., Popovic, N., Gresham, V. C., Wilson, E., Humphrey, J. D., 2010. Time course of carotid artery growth and remodeling in response to altered pulsatility. Am. J. Physiol. Heart Circ. Physiol. 299, 1875–1883.

Figueroa, C. A., Baek, S., Taylor, C. A., Humphrey, J. D., 2009. A computational framework for fluid-solid-growth modeling in cardiovascular simulations. Comput. Meth. Appl. Mech. Eng. 198, 3583–3602.

Figueroa, C. A., Vignon-Clementel, I. E., Jansen, K. C., Hughes, T. J., Taylor, C. A., 2006. A coupled momentum method for modeling blood flow in three-dimensional deformable arteries. Comput. Meth. Appl. Mech. Eng. 195, 5685–5706.

Gow, B. S., Hadfield, C. D., 1979. The elasticity of canine and human coronary arteries with reference to postmortem changes. Circ. Res. 45, 588–594.

Guyton, A. C., Hall, J. E. (Eds.), 2006. Textbook of Medical Physiology. Saunders, Philadelphia.

Hayashi, K., Hnada, H., Nagasawa, S., Okumura, A., Moritake, K., 1980. Stiffness and elastic behaviour of human intracranial and extracranial arteries. J. Biomech. 13, 175–184.

Hayenga, H. N., 2010. Mechanics of Atherosclerosis, Hypertension-Induced Growth, and Arterial Remodeling. Dissertation, Texas A&M University, TX.

Hu, J.-J., Ambrus, A., Fossum, T. W., Miller, M. W., Humphrey, J. D., Wilson, E., 2008. Time courses of growth and remodeling of porcine aortic media during hypertension: a quantitative immunohistochemical examination. J. Histochem. Cytochem. 56, 359–370.

Humphrey, J. D., 2002. Cardiovascular Solid Mechanics. Cells, Tissues, and Organs. Springer-Verlag, New York.

Kim, H. J., Vignon-Clementel, I. E., Coogan, J. S., Figueroa, C. A., Jansen, K. E., Taylor, C. A., 2010. Patient-specific modeling of blood flow and pressure in human coronary arteries. Ann. Biomed. Eng. 38, 3195–3209.

Kim, H. J., Vignon-Clementel, I. E., Figueroa, C. A., LaDisa, J. F., Jansen, K. E., Feinstein, J. A., Taylor, C. A., 2009a. On coupling a lumped parameter heart model and a three-dimensional finite element aorta model. Ann. Biomed. Eng. 37, 2153–2169.

Kim, T., Hwang, W., Kamm, R. D., 2009b. Computational analysis of a cross-linked actin-like network. Exp. Mech. 49, 91–104.

Lakatta, E. G., Wang, M., Najjar, S. S., 2009. Arterial aging and subclinical arterial disease are fundamentally intertwined at macroscopic and molecular levels. Med. Clin. North. Am. 93, 583–604.

Moireau, P., Xiao, N., Astorino, M., Figueroa, C. A., Chapelle, D., Taylor, C. A., Gerbeau, J.-F., 2012. External tissue support and fluid-structure simulation in blood flows. Biomech. Model. Mechanobiol. 11, 1–18.

Nichols, W. W., O'Rourke, M. F., 2005. McDonald's Blood Flow in Arteries. Theoretical, Experimental and Clinical Principles, 5th Edition. Arnold, London, Ch. 4, pp. 73–97.

O'Rourke, M. F., Hashimoto, J., 2007. Mechanical factors in arterial aging: A clinical perspective. J. Am. Coll. Cardiol. 50, 1–13.

Pearson, G. D., Devereux, R., Loeys, B., Maslen, C., Milewicz, D., Pyeritz, R., Ramirez, F., Rifkin, D., Sakai, L., Svensson, L., Wessels, A., Van Eyk, J., Dietz, H. C., National Heart, Lung, and Blood Institute and National Marfan Foundation Working Group, 2008. Report of the National Heart, Lung, and Blood Institute and National Marfan Foundation Working Group on Research in Marfan Syndrome and related disorders. Circulation 118, 785–791.

Redheuil, A., Yu, W.-C., Wu, C. O., Mousseaux, E., de Cesare, A., Yan, R., Kachenoura, N., Bluemke, D., Lima, J. A. C., 2010. Reduced ascending aortic strain and distensibility: earliest manifestations of vascular aging in humans. Hypertension 55, 319–326.

Safar, M. E., 2000. Pulse pressure, arterial stiffness, and cardiovascular risk. Curr. Opin. Cardiol. 15, 258–263.

Safar, M. E., 2010. Arterial aging-hemodynamic changes and therapeutic options. Nat. Rev. Cardiol. 7, 442–449.

Safar, M. E., Boudier, H. S., 2005. Vascular development, pulse pressure, and the mechanisms of hypertension. Hypertension 46, 205–209.

Sahni, O., Muller, J., Jansen, K. E., Shephard, M. S., Taylor, C. A., 2006. Efficient anisotropic adaptive discretization of the cardiovascular system. Comput. Meth. Appl. Mech. Eng. 195, 5634–5655.

Taylor, S. H., Donald, K. W., 1960. Circulatory studies at rest and during exercise in coarctation of the aorta before and after operation. Br. Heart J. 22, 117–139.

Vignon-Clementel, I. E., Figueroa, C. A., Jansen, K. E., Taylor, C. A., 2006. Outflow boundary conditions for three-dimensional finite element modeling of blood flow and pressure in arteries. Comput. Meth. Appl. Mech. Eng. 195, 3776–3796.

Wolinsky, H., 1972. Long-term effects of hypertension on the rat aortic wall and their relation to concurrent aging changes. Morphological and chemical studies. Circ. Res. 30, 301–309.

Xu, C., Zarins, C. K., Basiouny, H. S., Briggs, W. H., Reardon, C., Glagov, S., 2000. Defferential transmural distribution of gene expression for collagen types I and III proximal to aortic coarctation in the rabbit. J. Vasc. Res. 37, 170–182.

Index